Exploiting Cognition in ISAR Processing for Spectral Compatibility Applications

Massimo Rosamilia, *Member, IEEE*, Augusto Aubry, *Senior Member, IEEE*, Alessio Balleri, *Senior Member, IEEE*, Antonio De Maio, *Fellow, IEEE*, and Marco Martorella, *Fellow, IEEE*

***Abstract*—This article introduces and analyzes the concept of a cognitive inverse synthetic aperture radar (ISAR) ensuring spectral compatibility in crowded electromagnetic environments. In such a context, the proposed approach alternates between environmental perception, recognizing possible emitters in its frequency range, and an action stage, synthesizing and transmitting a tailored radar waveform to achieve the desired imaging task while guaranteeing spectral coexistence with overlaid emitters. The perception is carried out by a spectrum sensing module providing the true relevant spectral parameters of the sources in the environment. The action stage employs a tailored signal design process, synthesizing a radar waveform with bespoke spectral notches, enabling ISAR imaging over a wide spectral bandwidth without interfering with other radio frequency (RF) sources. A key enabling requirement for the proposed application is the capability to successfully recover possible missing data in the frequency domain (induced by spectral notches) and in the slow-time dimension (enabling concurrent RF activities still in a cognitive fashion). This process is carried out by resorting to advanced methods based on either the compressed-sensing framework or a rank-minimization (RM) recovery strategy. The capabilities of the proposed system are assessed by exploiting a dataset of drone measurements in the frequency band between 13 and 15 GHz. Results highlight the effectiveness of the devised architecture to enable spectral compatibility while delivering high-quality ISAR images as well as additional RF activities.**

***Index Terms*—Cognitive radar, compressed sensing (CS), drone imaging, inverse synthetic aperture radar (ISAR), ISAC, missing data, spectral compatibility.**

Received 17 June 2025; revised 30 September 2025 and 10 December 2025; accepted 14 December 2025. Date of publication 18 December 2025; date of current version 31 December 2025. The work of Massimo Rosamilia, Augusto Aubry, and Antonio De Maio was supported in part by the European Union under the Italian National Recovery and Resilience Plan (NRRP) of NextGenerationEU, partnership on "Telecommunications of the Future" (PE00000001-program "RESTART"). An earlier version of this paper was presented in part at the 2024 IEEE International Workshop on Technologies for Defense and Security (TechDefense) [DOI: 10.1109/TechDefense63521.2024.10863447]. *(Corresponding author: Antonio De Maio.)*

Massimo Rosamilia, Augusto Aubry, and Antonio De Maio are with the Department of Electrical Engineering and Information Technology (DIETI), Università degli Studi di Napoli "Federico II," 80125 Naples, Italy, and also with the National Inter-University Consortium for Telecommunications, 43124 Parma, Italy (e-mail: massimo.rosamilia@unina.it; augusto.aubry@unina.it; ademaio@unina.it).

Alessio Balleri is with the Centre for Defence Engineering and Physical Science, Cranfield University, Defence Academy of the United Kingdom, SN6 8LA Shrivenham, U.K. (e-mail: a.balleri@cranfield.ac.uk).

Marco Martorella is with the Department of Electronic, Electrical and Systems Engineering, University of Birmingham, B15 2TT Birmingham, U.K., and also with the Radar and Surveillance Systems (RaSS) National Laboratory of CNIT, 56124 Pisa, Italy (e-mail: marco.martorella@cnit.it).

Digital Object Identifier 10.1109/TRS.2025.3645384

I. Introduction

THE electromagnetic spectrum is a valuable and highly dynamic resource that is yet to be fully harnessed by radar systems [2]. Accordingly, an essential requirement for a next-generation radar system is the ability to operate in a congested electromagnetic spectral environment and guarantee compatibility with overlaid emitters by agility in the exploitation of the dynamically available frequency bands. Recent research emphasizes the importance of the waveform design and diversity paradigm [3], [4], [5], [6], [7] as a means of addressing this challenge. This approach, when implemented within a cognitive radar architecture, involves alternating between two key steps: a perception stage, where the radar detects emitters within its band of interest [8], [9], and an action stage, where a spectrally-shaped waveform is designed and transmitted to minimize interference with the aforementioned sources and to enhance spectrum efficiency by optimizing the signal-to-interference-plus-noise ratio (SINR) [2], [10], [11], [12], [13], [14], [15], [16].

While the open literature has mainly focused on radar detection, the present study shifts the focus to radar imaging. Specifically, this work proposes a cognitive inverse synthetic aperture radar (ISAR) imaging system with spectral compatibility requirements. As part of the radar operations workflow, a perception mode provides awareness of the emitters in the surrounding environment via specific radio frequency (RF) sensing modules [8], [9], [17]. This allows the synthesis and transmission of a tailored radar waveform encompassing spectral notches to avoid interference with overlaid systems, realizing the so-called *perception-action cycle*. Consequently, the radar is able to perform ISAR imaging over a wide bandwidth without inducing and experiencing interference from coexisting emitters.

Nevertheless, the presence of spectral notches in the transmitted waveform inevitably results in frequency domain gaps, which may eventually lead to spurious and high sidelobes in the resulting ISAR image if not adequately accounted for. Furthermore, in the context of a multifunction phased array radar (MPAR) system, wherein multiple tasks compete for the limited time slots, a tailored strategy to maximize the available resources (according to scheduling policies [18]) might assign noncontiguous or temporally uneven pulses to the imaging of a target, resulting in some slow-time domain gaps in the collected data. To overcome such drawbacks, a data recovery process is demanded at the image formation stage in order to

© 2025 The Authors. This work is licensed under a Creative Commons Attribution 4.0 License.
For more information, see https://creativecommons.org/licenses/by/4.0/

successfully accomplish ISAR imaging even in the presence of missing data in the frequency/slow-time domain [19], [20], [21], [22]. In the past decade, the compressed sensing (CS) framework has shown to be remarkably powerful in tackling this kind of problem, with numerous algorithms proposed in the open literature [23], [24], [25], [26]. In a nutshell, this strategy exploits the inherent property of the collected data exhibiting a sparse representation in some basis (e.g., Fourier) [27]. Notably, recent recovery algorithms leveraged on structures beyond conventional sparsity, such as group sparsity, low-rankness, etc., to regularize the inference process [26], [28], [29], [30], [31].

For the problem at hand, the well-known 2-D-SL0 algorithm [20], [22], [32] is applied to retrieve the missing data in the considered ISAR application. Furthermore, a low-rank recovery process is formulated to reconstruct the data based on the assumption of a limited number of dominant modes in the image. After approximating the rank with its tightest convex description, the problem is optimally solved by resorting to the iterative majorization–minimization (MM) algorithm [33], [34], [35].

To assess the performance of the proposed cognitive ISAR system, an extensive numerical analysis has been conducted employing a dataset of drone measurements in the frequency band [13, 15] GHz and HH polarization [36], [37]. The results highlight the radar capability to operate within a congested spectrum while producing high-quality ISAR images.

Summarizing, the main contributions of this article are as follows.

1) The ISAR imaging problem for spectral compatibility applications is introduced, and a transceiver architecture based on a cognitive paradigm is proposed and discussed.
2) A comprehensive theoretical description of the quadratically constrained quadratic program (QCQP)-based block waveform design algorithm, employed to synthesize spectrally compatible radar waveforms (action stage of the cognitive process), is provided. In addition, an in-depth case study for a cognitive ISAR waveform, designed under the assumption of two interferers, is presented, analyzing its power spectral density (PSD) estimate and autocorrelation behavior.
3) The ISAR image formation problem under missing data, due to spectral compatibility constraints, is formulated, and two solution strategies are assessed. The former relies on a standard CS-based algorithm, whereas the latter employs an alternative recovery method based on rank-minimization (RM), solved through the MM algorithm.
4) Extensive experimental analysis is carried out using measured drone data, considering several scenarios of practical relevance. The ISAR results are visually compared with the ground truth (GT) (i.e., imaging without spectral coexistence constraints), and the reconstruction performance is numerically evaluated using three quality metrics: image contrast (IC), image coherence (COH), and normalized mean squared error (NMSE).

The remainder of this work is organized as follows. Section II introduces the waveform design framework for spectral compatibility applications. Section III discusses the ISAR imaging technique in the presence of incomplete data in the frequency/slow-time domain by presenting two recovery strategies based on the CS framework and RM, respectively. In Section IV, extensive numerical analysis on a dataset comprising returns from a commercial drone is reported and discussed considering several scenarios of practical relevance. Finally, Section V concludes the article.

A. Notation

Boldface is used for vectors $\boldsymbol{a}$ (lower case), and matrices $\boldsymbol{A}$ (upper case). The nth element of $\boldsymbol{a}$ and the (m,l)th entry of $\boldsymbol{A}$ are, respectively, denoted by $\boldsymbol{a}(n)$ and $\boldsymbol{A}(m,l)$. The transpose, the conjugate, and the conjugate transpose operators are denoted by the symbols $(\cdot)^{\mathrm{T}}$, $(\cdot)^{\star}$, and $(\cdot)^{\dagger}$, respectively. $\odot$ represents the Hadamard (element-wise) product. $\mathbb{C}^N$ is the set of N-dimensional vectors of complex numbers. Furthermore, $\mathbf{1}$ is the vector with all elements being one. For any complex number x, $|x|$ indicates the modulus of x. For any matrix $\boldsymbol{A}$, $\|\boldsymbol{A}\|_0$, $\|\boldsymbol{A}\|_1$, $\|\boldsymbol{A}\|_F$, and $\|\boldsymbol{A}\|_{\star}$ denote the corresponding ℓ_0, ℓ_1, Frobenius, nuclear norm, respectively, whereas $(\boldsymbol{A})^{+}$ represents its pseudoinverse. In addition, $\|\boldsymbol{A}\|_{\max} = \max_{m,l} |\boldsymbol{A}(m,l)|$ is the max norm of $\boldsymbol{A}$. Moreover, for any real matrix $\boldsymbol{B}$, $(\boldsymbol{B})_{+}$ denotes the rectified linear unit operator, which replaces all negative entries of $\boldsymbol{B}$ with zero. For any real number a, $\lceil a \rceil$ yields the least integer greater than or equal to a. In addition, the rank and the Shannon-rank [38] of $\boldsymbol{A}$ are denoted by $\mathrm{rank}\{A\}$ and $\mathrm{rank}_S\{A\}$, respectively, where $\mathrm{rank}_S\{\boldsymbol{A}\} = \exp\left[-\sum_{i=1}^{r}(\sigma_i(\boldsymbol{A}))/(\|\boldsymbol{\sigma}\|_1)\log((\sigma_i(\boldsymbol{A}))/(\|\boldsymbol{\sigma}\|_1))\right]$ with $\boldsymbol{\sigma} = [\sigma_1(\boldsymbol{A}), \ldots, \sigma_r(\boldsymbol{A})]^{\mathrm{T}}$ the vector comprising the singular values of $\boldsymbol{A}$. Finally, $\mathbb{A}[\cdot]$ represents the spatial mean operator, whereas the letter j represents the imaginary unit (i.e., $j = (-1)^{1/2}$).

II. Waveform Design for Spectral Compatibility

In this section, the problem of designing spectrally-shaped waveforms is briefly introduced with reference to a cognitive radar system.

To this end, let us consider a radar operating in the presence of K emitters, each of them transmitting over a frequency band $\Omega_k = [f_1^k, f_2^k], k = 1, \ldots, K$, within the radar frequency support range, where f_1^k and f_2^k denote the lower and upper normalized frequencies (with respect to the sampling rate) for the kth source, respectively.

Let $c(t)$ be the baseband equivalent of the radar transmitted waveform whose complex sequence $\boldsymbol{c}$ (corresponding to samples of $c(t)$ picked up at the frequency rate equal to the radar bandwidth) is $c(i)$, $i = 1, \ldots, N$. To ensure spectral compatibility with the overlaid emitters, the cognitive radar has to suitably shape the spectrum of the transmitted signal to manage the amount of interfering energy produced in the shared frequency intervals. The average signal energy transmitted on the kth band Ω_k is given by [14]

$$\frac{1}{f_2^k - f_1^k}\int_{f_1^k}^{f_2^k} S_c(f)\,df \tag{1}$$

where

$$S_c(f) = \left| \sum_{n=1}^{N} c(n) e^{-j2\pi f(n-1)} \right|^2 = N \left| \boldsymbol{c}^\dagger \boldsymbol{p}_f \right|^2 \tag{2}$$

with

$$\boldsymbol{p}_f = \frac{1}{\sqrt{N}} \left[1, \exp(-j2\pi f), \ldots, \exp(-j2\pi (N-1) f)\right]^{\mathrm{T}} \tag{3}$$

the temporal steering vector tuned to the normalized frequency f. That said, each frequency band Ω_k is substantially discretized by taking the normalized frequencies $f_i = i/N$, $i = 0, \ldots, N-1$ falling in Ω_k itself. Then, denoting by

$$\boldsymbol{F}_N(m,n) = \frac{1}{\sqrt{N}} e^{-\frac{j2\pi(m-1)(n-1)}{N}} \tag{4}$$

the $N \times N$ Fourier matrix scaled by $1/\sqrt{N}$, a viable means to quantify the average energy level injected on Ω_k is through

$$\frac{N\Delta f}{f_2^k - f_1^k} \sum_{f_i \in \Omega_k} \left| \boldsymbol{c}^\dagger \boldsymbol{p}_{f_i} \right|^2 = \frac{1}{f_2^k - f_1^k} \sum_{f_i \in \Omega_k} \left| \boldsymbol{c}^\dagger \boldsymbol{p}_{f_i} \right|^2 = \boldsymbol{c}^\dagger \boldsymbol{R}_N^k \boldsymbol{c} \tag{5}$$

where[1]

$$\boldsymbol{R}_N^k = \frac{1}{f_2^k - f_1^k} \boldsymbol{Q}_N^k \boldsymbol{Q}_N^{k\,\dagger} \tag{6}$$

and $\boldsymbol{Q}_N^k$ is the submatrix of $\boldsymbol{F}_N$ whose columns correspond to the discrete frequencies in the interval Ω_k.

Thus, indicating by E_I^k, $k = 1, \ldots, K$, the acceptable level of interference on Ω_k, which is related to the quality of service demanded by the kth licensed emitter,[2] the transmitted radar waveform has to comply with the constraints

$$\boldsymbol{c}^\dagger \boldsymbol{R}_N^k \boldsymbol{c} \le E_I^k, \quad k = 1, \ldots, K. \tag{7}$$

By doing so, a detailed control of the interference energy produced on each shared frequency bandwidth is enforced.

In the following, a waveform design algorithm for spectral compatibility applications is presented, which complies with the aforementioned spectral constraints.

A. QCQP-Based Block Waveform Design

As previously mentioned, the purpose of the action stage in the considered cognitive radar architecture is to synthesize a bespoke radar waveform in order to control the amount of transmitted energy on overlaid transmitters. To this end, it is assumed that at the perception stage, the cognitive radar gathers true spectral knowledge on the sources operating in its frequency band through a spectrum sensing module that periodically monitors the RF environment [8], [17].

Leveraging the information from the perception stage, a suitable signal is generated using a waveform design algorithm and is transmitted via the radar antenna toward the target location. A bespoke algorithm, inspired by [14] (in the sense that it inherits the formulation of the spectral constraints), is now proposed, which relies on a QCQP formulation attempting to control the amount of interfering energy produced in the frequency intervals occupied by overlaid EM sources, while maximizing the similarity with a reference signal.

Precisely, the similarity with a standard chirp signal $\boldsymbol{c}_0$ (tailored for the ISAR requirements in terms of spectral bandwidth) is considered as a figure of merit, in order to perform the spectral shaping of the cognitive waveform. Hence, by partitioning the waveform to synthesize in L smaller blocks of size $\bar{N}$ (assuming, without loss of generality, that $N = L\bar{N}$), i.e.,

$$\boldsymbol{c} = \left[\boldsymbol{c}_1^{\mathrm{T}}, \ldots, \boldsymbol{c}_L^{\mathrm{T}}\right]^{\mathrm{T}}, \tag{8}$$

the design approach is tantamount to minimizing the distance $\|\boldsymbol{c} - \boldsymbol{c}_0\|^2$ and can be formulated as the following QCQP convex optimization problem:

$$\mathcal{P} \begin{cases} \min\limits_{\boldsymbol{c} \in \mathbb{C}^N} & \|\boldsymbol{c} - \boldsymbol{c}_0\|^2 \\ \text{s.t.} & \|\boldsymbol{c}_l\|^2 \le 1/L, \; l = 1, \ldots, L \\ & \boldsymbol{c}^\dagger \boldsymbol{R}_N^k \boldsymbol{c} \le E_I^k, \; k = 1, \ldots K \end{cases} \tag{9}$$

whose optimal solution can be obtained in polynomial time with arbitrary precision. The norm constraint imposed on the individual blocks $\boldsymbol{c}_i$ of the sequence $\boldsymbol{c}$ is aimed at ensuring a bound on the transmitted energy, along with the avoidance of possible energy imbalances of different segments in the time domain.

In a practical wideband scenario where the waveform length N is much larger than 10^4, computing a solution to $\mathcal{P}$ involves handling a rather high computational and space complexity (i.e., demanding the storage of large matrices). In such instances, this drawback can be potentially addressed by sequentially optimizing each block $\boldsymbol{c}_l$, $l = 1, \ldots, L$, leading to a (generally) suboptimal and computationally tractable design process. By partitioning the reference code $\boldsymbol{c}_0$ in L blocks of length $\bar{N}$, i.e.,

$$\boldsymbol{c}_0 = \left[\boldsymbol{c}_{0,1}^{\mathrm{T}}, \ldots, \boldsymbol{c}_{0,l}^{\mathrm{T}}, \ldots, \boldsymbol{c}_{0,L}^{\mathrm{T}}\right]^{\mathrm{T}} \tag{10}$$

the design of the lth sub-block involves the maximization of the similarity with the reference signal segment $\boldsymbol{c}_{0,l}$ while satisfying tailored spectral constraints for the considered block, i.e.,

$$\boldsymbol{c}_l^\dagger \boldsymbol{R}_{\bar{N}}^k \boldsymbol{c}_l \le E_I^k / L, \quad k = 1, \ldots, K. \tag{11}$$

Nevertheless, synthesizing each block $\boldsymbol{c}_l$ independently leads to a lack of control of the spectral behavior between consecutive blocks. To guarantee a smooth transition between the subsequent blocks of samples and avoid possible spectral spurious, a heuristic but effective solution technique is now illustrated. Specifically, the sequence $\boldsymbol{c}$ is progressively designed by employing a set of partially overlapped time windows (i.e., blocks) each including a segment of the signal already synthesized and a segment to be optimized. Accordingly, denoting by $\boldsymbol{c}_{l-1,W}$ the vector composed of the last $W \in [0, \bar{N}/2]$ elements of $\boldsymbol{c}_{l-1}$, i.e., the signal block already designed, the optimization process reformulates the quadratic

[1] Unless otherwise specified, the subscript N in $\boldsymbol{F}_N$, $\boldsymbol{Q}_N$, and $\boldsymbol{R}_N^k$ denotes the number of rows and represents the number of points used to discretize the frequency interval $[0, 1]$.

[2] As discussed in [39], the amount of interference E_I^k injected into the kth stopband can be set to guarantee an appropriate quality of service for the coexisting telecommunication system. In particular, based on the power estimated at the radar end, E_I^k should be constrained such that the resulting signal-to-interference ratio of the kth system remains above the minimum threshold required for reliable operation. Further details can be found in [39] and [40].

constraints in terms of $\tilde{\boldsymbol{c}} = [\boldsymbol{c}_{l-1,W}^{\mathrm{T}}, \check{\boldsymbol{c}}_l^{\mathrm{T}}]^{\mathrm{T}} \in \mathbb{C}^{\bar{N}}$, with $\check{\boldsymbol{c}}_l$ the segment to optimize at the current step (of size $\bar{N} - W$).

Moreover, the total number of optimizations to perform (in addition to the one pertaining to the first block) is equal to $\tilde{L} = \lceil (N - \bar{N})/(\bar{N} - W) \rceil$.

By leveraging the aforementioned guidelines, the waveform design problem for the first and the lth (with $l = [2, \ldots, \tilde{L} + 1]$) block can be formulated as the following QCQP convex optimization problems:

$$\mathcal{P}_1 \begin{cases} \min\limits_{\check{\boldsymbol{c}}_1 \in \mathbb{C}^{\bar{N}}} & \left\| \check{\boldsymbol{c}}_1 - \bar{\boldsymbol{c}}_{0,1} \right\|^2 \\ \text{s.t.} & \|\check{\boldsymbol{c}}_1\|^2 \le 1/L \\ & \check{\boldsymbol{c}}_1^{\dagger} \boldsymbol{R}_{\bar{N}}^k \check{\boldsymbol{c}}_1 \le E_I^k / L,\ k = 1, \ldots K \end{cases} \tag{12}$$

and

$$\mathcal{P}_l \begin{cases} \min\limits_{\check{\boldsymbol{c}}_l \in \mathbb{C}^{\bar{N}-W}} & \left\| \check{\boldsymbol{c}}_l - \bar{\boldsymbol{c}}_{0,l} \right\|^2 \\ \text{s.t.} & \tilde{\boldsymbol{c}} = \left[\boldsymbol{c}_{l-1,W}^{\mathrm{T}}, \check{\boldsymbol{c}}_l^{\mathrm{T}} \right]^{\mathrm{T}} \\ & \|\tilde{\boldsymbol{c}}\|^2 \le 1/L \\ & \tilde{\boldsymbol{c}}^{\dagger} \boldsymbol{R}_{\bar{N}}^k \tilde{\boldsymbol{c}} \le E_I^k / L,\ k = 1, \ldots K \end{cases} \tag{13}$$

respectively, where the reference code $\boldsymbol{c}_0$ is partitioned in $\tilde{L}+1$ blocks as

$$\boldsymbol{c}_0 = \left[\bar{\boldsymbol{c}}_{0,1}^{\mathrm{T}}, \bar{\boldsymbol{c}}_{0,2}^{\mathrm{T}}, \ldots, \bar{\boldsymbol{c}}_{0,\tilde{L}+1}^{\mathrm{T}} \right]^{\mathrm{T}} \tag{14}$$

with $\bar{\boldsymbol{c}}_{0,1}$ of size $\bar{N}$ and $\bar{\boldsymbol{c}}_{0,l}$ of size $(\bar{N} - W)$, $l = 2, \ldots, \tilde{L} + 1$. Remarkably, (12) and (13) can be practically handled as they are computationally and space efficient.

Algorithm 1 QCQP Block Waveform Design for Cognitive Radar

Input: N, $\bar{N}$, W, $\{\boldsymbol{R}_{\bar{N}}^k\}_{k=1}^K$, $\{E_I^k\}_{k=1}^K$, $\boldsymbol{c}_0$.
1 set $L = \lceil N/\bar{N} \rceil$ and $\tilde{L} = \lceil (N - \bar{N})/(\bar{N} - W) \rceil$;
2 partition $\boldsymbol{c}_0$ in $\tilde{L} + 1$ blocks as $\boldsymbol{c}_0 = [\bar{\boldsymbol{c}}_{0,1}^{\mathrm{T}}, \bar{\boldsymbol{c}}_{0,2}^{\mathrm{T}}, \ldots, \bar{\boldsymbol{c}}_{0,\tilde{L}+1}^{\mathrm{T}}]^{\mathrm{T}}$, with $\bar{\boldsymbol{c}}_{0,1}$ of size $\bar{N}$ and $\bar{\boldsymbol{c}}_{0,l}$ of size $(\bar{N} - W)$, $l = 2, \ldots, \tilde{L} + 1$;
3 compute $\boldsymbol{c}_1$ as a solution to (12);
4 **for** $l = [2, \ldots, \tilde{L} + 1]$ **do**
5 compute $\boldsymbol{c}_l$ as a solution to (13);
6 **end**
Output: $\boldsymbol{c} = [\boldsymbol{c}_1^{\mathrm{T}}, \ldots, \boldsymbol{c}_{\tilde{L}+1}^{\mathrm{T}}]^{\mathrm{T}}$

Summarizing, by combining block-wise optimization with different segments of the reference sequence and tailored spectral constraints, the proposed approach exhibits an affordable computational effort while satisfying the spectral requirements and effectively mimicking the characteristics of the reference waveform. Algorithm 1 specifies the proposed block-wise waveform design strategy for the considered cognitive ISAR system operating to guarantee spectral coexistence with other emitters.

B. Analysis of the Cognitive-Based Spectral Compatible ISAR Waveform

In the following, a waveform synthesized with Algorithm 1 is analyzed in terms of spectral features and autocorrelation behavior. At the synthesis stage, a radar bandwidth of 2 GHz and a waveform duration of 5 μs, are considered as system parameters, with a standard chirp used as reference signal $\boldsymbol{c}_0$. The synthesis of the spectral compatible waveform is performed via Algorithm 1 using block size $\bar{N} = 5000$ and $W = 2500$. For the cognitive application, two licensed emitters are assumed operating in the environment, on the intervals [13.38, 13.62] and [14.53, 14.65] GHz, respectively. Consequently, stop-bands have been employed for spectral shaping, with a notch depth of 40 and 30 dB, respectively.

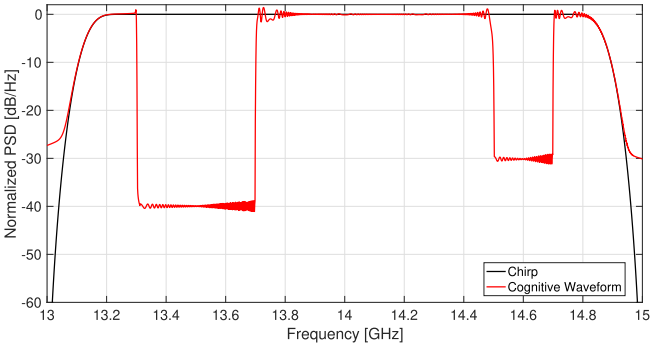

Fig. 1. PSD estimate of the reference (chirp) waveform and the synthesized one via Algorithm 1 (using block size $\bar{N} = 5000$). The PSDs are estimated using the Welch method (considering segments of 3000 samples with 2900 samples of overlap from segment to segment, weighted with a Blackman–Harris window and normalized to the mean value of the reference waveform PSD.

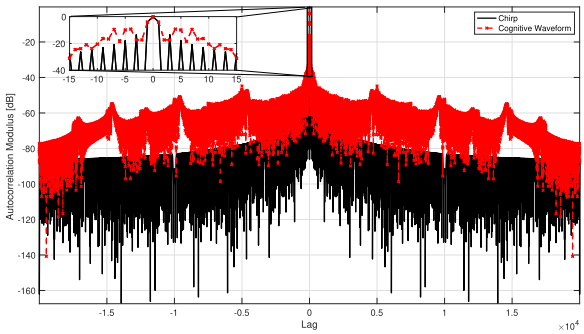

Fig. 2. Normalized autocorrelation of the reference and the synthesized waveforms.

Fig. 1 reports the PSD of the reference waveform $\boldsymbol{c}_0$ and the cognitive one synthesized using Algorithm 1. The PSDs are estimated using the Welch method, considering segments of 3000 samples, with 2900 samples of overlap from segment to segment, weighted with a Blackman–Harris window. Moreover, the PSDs are normalized to the maximum PSD value of the reference waveform. The figure clearly shows that the designed waveform exhibits spectral notches almost perfectly lined-up within the desired stop-bands, while still adhering to the reference waveform on the passband intervals. Moreover, the figure highlights that the resulting notches depth is approximately -40 and -30 dB, with some (limited) spurious near the boundaries of the stop-bands.

To quantify the characteristics of the designed spectrally-notched radar signal, Fig. 2 compares the amplitude of its autocorrelation function (AF) (normalized to the peak) with that of the reference signal. The results pinpoint that the

obtained radar sequence is characterized by an autocorrelation peak sidelobe level (PSL) of −9.5 dB, while for the reference waveform it is equal to −13 dB, with an actual offset of about 3.5 dB. Furthermore, the designed waveform successfully achieves the desired spectral shaping while maintaining the AF 3-dB mainlobe almost unaltered, matching its reference counterpart.

III. ISAR Imaging in the Presence of Missing Data

ISAR imaging is a technique used to generate high-resolution images of moving targets. Conventional imaging techniques rely on the coherent integration of received echoes over a range of aspect angles, generally resorting to Fourier-based methods (downstream, a careful compensation stage). However, in the presence of missing samples in the frequency domain, for instance due to spectral notches in the transmitted waveform, ISAR images obtained with the standard range-Doppler (RD) algorithm [42] may be distorted or exhibit a coarse final image resolution due to the degradation of the matched filter response. Therefore, to provide high-quality images in this context, the processing stage could include a strategy to retrieve any missing measurements within the available collected data. In particular, let $\boldsymbol{S}$ be[3] the observed *incomplete* matrix in the slow-time/frequency domain (where zeros are present in locations where either a frequency or a pulse is missed) and $\boldsymbol{I}$ the ISAR image; then, the goal is to minimize the displacement term (quantified via the Frobenius norm), i.e.,

$$\min_{\boldsymbol{I}} \left\| \boldsymbol{S} - \boldsymbol{\Theta}_x \boldsymbol{I} \boldsymbol{\Theta}_y^{\dagger} \right\|_F^2 \tag{15}$$

where $\boldsymbol{\Theta}_x$ and $\boldsymbol{\Theta}_y$ are the corresponding undercomplete Fourier matrices (obtained by zeroing specific rows of the DFT matrix corresponding to the missing frequencies/pulses samples) [20], which can be computed starting from the parameters of the cognitive waveform spectral notches and the location of the temporal gaps. Unfortunately, Problem (15) is ill-posed since the missing entries of $\boldsymbol{S}$ cannot be uniquely determined without making assumptions on the matrix $\boldsymbol{I}$, namely multiple solutions to Problem (15), each producing a different filling of the missed measurements, exist. A viable method to overcome this limitation is to introduce another figure of merit to assess the quality of the different feasible solutions, which is usually referred to as regularization process in the open literature [45], [46], [47] and amounts to substantially limit the solution state space. Otherwise stated, the inference task can be reformulated as a bi-objective optimization problem, where one figure of merit is the squared norm of the displacement, while the other is a regularization function. As to the latter, in the open literature the ℓ_0 norm of $\boldsymbol{I}$ has been employed, and the bi-objective problem is handled by minimizing it under a constraint on the maximum amount of displacement. In this regard, the CS framework (with bespoke approximations of the ℓ_0 norm) has been successfully applied to this retrieval problem (see Section III-A). An alternative method is to consider the rank of $\boldsymbol{I}$ as the regularization term and to tackle the optimization problem via the scalarization framework [48] (see Section III-B).

Finally, after the reconstruction stage, performed by means of CS-based (Section III-A) or RM-based (Section III-B) algorithms, it is possible to reconstruct the slow-time/frequency domain data matrix. In particular, leveraging the conventional Fourier dictionaries $\boldsymbol{\Psi}_x$ and $\boldsymbol{\Psi}_y$ that account for the range compression and the cross-range compression, respectively, the data is reconstructed as

$$\hat{\boldsymbol{S}}_c = \boldsymbol{\Psi}_x \hat{\boldsymbol{I}} \boldsymbol{\Psi}_y^{\dagger} \tag{16}$$

which allows to realize the ISAR imaging by means of the conventional RD algorithm applied on $\hat{\boldsymbol{S}}_c$ [20].

A. Compressed-Sensing Recovery

CS represents a powerful signal processing tool capable of reconstructing signals from a small amount of measurements [49]. It has been successfully applied to accomplish ISAR imaging, yielding noteworthy improvements in the context of data reduction as well as resolution enhancement [20]. The key principle underlying CS-based ISAR imaging lies in its ability to leverage the sparsity assumption of scatterers in the image domain. From a physical point of view, at high frequencies, a radar signal is sparse in the image domain (i.e., when represented in the 2-D Fourier basis), since it can be accurately described by the superposition of a few prominent scatterer responses in the radar image plane [20].

Accordingly, the CS approach reconstructs the ISAR image $\boldsymbol{I}$ by solving the following optimization problem:

$$\begin{aligned} \hat{\boldsymbol{I}} &= \arg\min_{\boldsymbol{I}} \|\boldsymbol{I}\|_0 \\ &\text{s.t.} \quad \left\| \boldsymbol{S} - \boldsymbol{\Theta}_x \boldsymbol{I} \boldsymbol{\Theta}_y^{\dagger} \right\|_F^2 \le \epsilon \end{aligned} \tag{17}$$

where ϵ is a user-defined tuning parameter accounting for the noise level in the measured data.

Algorithm 2 2-D-SL0 Algorithm

Input: $\boldsymbol{\Theta}_x$, $\boldsymbol{\Theta}_y$, $\boldsymbol{S}$, $\sigma_{\min}$, α, μ_0, L.
Compute $\boldsymbol{\Theta}_x^{+}$ and $\boldsymbol{\Theta}_y^{+}$;
Compute the initial estimate: $\boldsymbol{I} = \boldsymbol{\Theta}_x^{+} \boldsymbol{S} (\boldsymbol{\Theta}_y^{+})^{\dagger}$;
Set $\sigma = 2 \|\boldsymbol{I}\|_{\max}$;
while $\sigma > \sigma_{\min}$ **do**
  for $i = 1$ **to** L **do**
    Update: $\boldsymbol{D} = \boldsymbol{I} \odot \boldsymbol{G}$, with $\boldsymbol{G}(m,n) = \exp(-\frac{|\boldsymbol{I}(m,n)|^2}{2\sigma^2})$;
    Gradient step: $\boldsymbol{I} = \boldsymbol{I} - \mu_0 \boldsymbol{D}$;
    Projection: $\boldsymbol{E} = \boldsymbol{\Theta}_x^{+}(\boldsymbol{\Theta}_x \boldsymbol{I} \boldsymbol{\Theta}_y^{\dagger} - \boldsymbol{S})(\boldsymbol{\Theta}_y^{+})^{\dagger}$;
    Update: $\boldsymbol{I} = \boldsymbol{I} - \boldsymbol{E}$;
  end
  Update $\sigma = \alpha\sigma$;
end
Output: $\hat{\boldsymbol{I}} = \boldsymbol{I}$

Notably, in [20], the 2-D-SL0 algorithm [22] has been successfully employed to handle (17), obtaining a sparse solution consistent with the observed data. The procedure is summarized in Algorithm 2, where, unless otherwise specified, $\sigma_{\min} = 10^{-6}, \alpha = 0.6, \mu_0 = 2$, and $L = 15$.

[3]Note that a tailored preprocessing step (also accounting for the presence of possible missing data) is assumed to be already carried out to compensate for the translational component in the measured signals [43], [44].

B. RM Recovery

In this subsection, a different regularization function is considered, i.e., the rank of $\boldsymbol{I}$, which rules the number of modes describing the image. As a consequence, the figure of merit involved in the inference problem is as follows.

1) $\|\boldsymbol{S}-\boldsymbol{\Theta}_x\boldsymbol{I}\boldsymbol{\Theta}_y^\dagger\|_F^2$, which controls the fitting of the recovered image with the available measurements.
2) rank$\{\boldsymbol{I}\}$, which accounts for the amount of modes required to faithfully describe the image.

Hence, to face the resulting bi-objective optimization, as already mentioned, the scalarization framework [48] is exploited. Precisely, the ISAR image retrieval is formulated as

$$\hat{\boldsymbol{I}} = \arg\min_{\boldsymbol{I}} \frac{1}{2}\left\|\boldsymbol{S}-\boldsymbol{\Theta}_x\boldsymbol{I}\boldsymbol{\Theta}_y^\dagger\right\|_F^2 + \lambda \text{rank}\{\boldsymbol{I}\} \tag{18}$$

which is an unconstrained single-objective optimization problem with λ the corresponding weight parameter that rules the tradeoff between the displacement and the regularization terms.

It is important to observe that Problem (18) is NP-hard (due to the rank term) [31]. Hence, to determine a high-quality suboptimal solution, the rank operator is approximated via the plain nuclear norm, which is the closest convex relaxation to the rank function [31], [50], [51]. According to the above guidelines, the inference problem becomes

$$\hat{\boldsymbol{I}} = \arg\min_{\boldsymbol{I}} f(\boldsymbol{I}),\ f(\boldsymbol{I}) \triangleq \frac{1}{2}\left\|\boldsymbol{S}-\boldsymbol{\Theta}_x\boldsymbol{I}\boldsymbol{\Theta}_y^\dagger\right\|_F^2 + \lambda\|\boldsymbol{I}\|_\star \tag{19}$$

which is a convex optimization problem. A viable strategy to minimize the objective in (19) relies on the MM framework, which is a powerful iterative procedure capable of addressing challenging optimization problems in an efficient and scalable way (see [35], [52], [53] for technical details). The method involves the construction of a tailored surrogate function (s.f.) that satisfies specific properties, leveraging on the optimized solution from the previous iteration. The s.f. is then minimized to update the optimized point.

To proceed further, let us denote by $\boldsymbol{I}_k$ the estimate of $\boldsymbol{I}$ at the kth iteration; following similar line of reasoning as in [31], a s.f. $g(\boldsymbol{I};\boldsymbol{I}_k)$ for the objective function in (19) is given by the quadratic approximation of $f(\boldsymbol{I})$, i.e.,

$$g(\boldsymbol{I};\boldsymbol{I}_k) = \frac{\tau}{2}\left\|\boldsymbol{I}-\bar{\boldsymbol{I}}_k\right\|_F^2 + \lambda\|\boldsymbol{I}\|_\star + f(\boldsymbol{I}_k) - \frac{1}{2\tau}\|\nabla f(\boldsymbol{I}_k)\|_F^2 \tag{20}$$

where $\tau \geq \mathcal{L}_f \triangleq \lambda_{\max}(\boldsymbol{C}^\dagger\boldsymbol{C}) = \lambda_{\max}(\boldsymbol{\Theta}_x^\dagger\boldsymbol{\Theta}_x)\lambda_{\max}(\boldsymbol{\Theta}_y^\dagger\boldsymbol{\Theta}_y)$ [31], with $\boldsymbol{C} = \boldsymbol{\Theta}_y^\star \otimes \boldsymbol{\Theta}_x$,

$$\bar{\boldsymbol{I}}_k = \boldsymbol{I}_k - \frac{1}{\tau}\boldsymbol{\Theta}_x^\dagger\left(\boldsymbol{\Theta}_x\boldsymbol{I}_k\boldsymbol{\Theta}_y^\dagger - \boldsymbol{S}\right)\boldsymbol{\Theta}_y \tag{21}$$

whereas $\nabla f(\boldsymbol{I}_k)$ is the gradient of $f(\boldsymbol{I})$ evaluated at $\boldsymbol{I}_k$.

Let us now focus on the minimization of $g(\boldsymbol{I};\boldsymbol{I}_k)$. To this end, let $\boldsymbol{U}_k\boldsymbol{\Sigma}_k\boldsymbol{V}_k^\dagger$ be the singular value decomposition (SVD) of $\bar{\boldsymbol{I}}_k$ and $\boldsymbol{U}\boldsymbol{\Sigma}\boldsymbol{V}^\dagger$ that of $\boldsymbol{I}$, with the singular values in $\boldsymbol{\Sigma}_k$ and $\boldsymbol{\Sigma}$ sorted in descending order; hence, based on [54, Corollary 7.4.1.5],

$$\left\|\boldsymbol{I}-\bar{\boldsymbol{I}}_k\right\|_F^2 \geq \|\boldsymbol{\Sigma}-\boldsymbol{\Sigma}_k\|_F^2 \tag{22}$$

with the equality if $\boldsymbol{I} = \boldsymbol{U}_k\boldsymbol{\Sigma}\boldsymbol{V}_k^\dagger$. As a consequence, the left and right singular vectors of a minimizer for the objective in (20) are the same as $\bar{\boldsymbol{I}}_k$. Therefore, assuming that $\bar{\boldsymbol{I}}_k$ has r nonzero singular values $\{\bar{\sigma}_k^{(i)}\}_{i=1}^r$, the optimization problem at hand reduces to computing the singular values as solution of the optimization problem

$$\min_{\sigma^{(1)}\geq 0,\ldots,\sigma^{(r)}\geq 0} \tilde{g}(\boldsymbol{I};\boldsymbol{I}_k) \triangleq \sum_{i=1}^{r}\left[\frac{\tau}{2}\left(\sigma^{(i)}-\bar{\sigma}_k^{(i)}\right)^2 + \lambda\sigma^{(i)}\right] \tag{23}$$

where $\sigma^{(i)}, i = 1,\ldots,r$, are the possible non zero singular values of $\boldsymbol{I}$. In addition, since the problem is separable in its variables, the ith singular value of $\boldsymbol{I}$ can be computed solving

$$\min_{\sigma^{(i)}\geq 0} \frac{\tau}{2}\left(\sigma^{(i)}-\bar{\sigma}_k^{(i)}\right)^2 + \lambda\sigma^{(i)}, \quad i = 1,\ldots,r \tag{24}$$

whose optimal value is given by

$$\sigma^{(i)} = \left(\bar{\sigma}_k^{(i)} - \frac{\lambda}{\tau}\right)_+. \tag{25}$$

Summarizing, a minimizer of (20) is

$$\boldsymbol{I}_{k+1} = \boldsymbol{U}_k\boldsymbol{\Sigma}_{k+1}\boldsymbol{V}_k^\dagger \tag{26}$$

with $\boldsymbol{\Sigma}_{k+1}$ a diagonal matrix whose ith diagonal element is $\sigma^{(i)}$.

Algorithm 3 MM-Based RM Algorithm

Input: $\boldsymbol{I}_0$, λ, $\boldsymbol{S}$, $\boldsymbol{\Theta}_x$, $\boldsymbol{\Theta}_y$, $k = k_{\text{MAX}}$.
set $\tau \geq \lambda_{max}(\boldsymbol{\Theta}_x^\dagger\boldsymbol{\Theta}_x)\lambda_{max}(\boldsymbol{\Theta}_y^\dagger\boldsymbol{\Theta}_y)$;
set $k = 0$;
set $\boldsymbol{I}_M = \boldsymbol{\Theta}_x^+\boldsymbol{S}(\boldsymbol{\Theta}_y^\dagger)^+$;
repeat
  set $\bar{\boldsymbol{I}}_k = \boldsymbol{I}_k - \frac{1}{\tau}\boldsymbol{\Theta}_x^\dagger(\boldsymbol{\Theta}_x\boldsymbol{I}_k\boldsymbol{\Theta}_y^\dagger - \boldsymbol{S})\boldsymbol{\Theta}_y$;
  compute the SVD of $\bar{\boldsymbol{I}}_k$: $\bar{\boldsymbol{I}}_k = \boldsymbol{U}_k\boldsymbol{\Sigma}_k\boldsymbol{V}_k^\dagger$;
  set $\sigma^{(i)} = (\bar{\sigma}_k^{(i)} - \frac{\lambda}{\tau})_+$, with $\bar{\sigma}_k^{(i)}$ the non-zero singular values of $\bar{\boldsymbol{I}}_k$;
  set $\boldsymbol{I}_{k+1} = \boldsymbol{U}_k\boldsymbol{\Sigma}_{k+1}\boldsymbol{V}_k^\dagger$, with $\boldsymbol{\Sigma}_{k+1}$ a diagonal matrix whose ith diagonal element is $\sigma^{(i)}$;
  set $k = k+1$;
until rank$_S\{\boldsymbol{I}_k\} \leq$ rank$_S\{\boldsymbol{I}_M\}$ *or* $k = k_{\text{MAX}}$;
Output: $\hat{\boldsymbol{I}} = \boldsymbol{I}_k$

The overall procedure is detailed in Algorithm 3, wherein $\boldsymbol{I}_0$ is the initialization matrix (e.g., the output of the 2-D-SL0 algorithm). Finally, denoting by $\boldsymbol{I}_M = \boldsymbol{\Theta}_x^+\boldsymbol{S}(\boldsymbol{\Theta}_y^\dagger)^+$ the ISAR image computed on the incomplete data, the procedure terminates when either the condition rank$_S\{\boldsymbol{I}_k\} \leq$ rank$_S\{\boldsymbol{I}_M\}$ is met or the maximum number of iterations k_{MAX} is reached.

IV. Numerical Analysis

In this section, the effectiveness of the proposed procedure is investigated by comparing the image obtained with the proposed cognitive ISAR process with those resulting from an ideal case (receiving only the useful target contribution without spectral holes) as well as a standard ISAR operating in the presence of interference. The comparison is conducted both visually and numerically by resorting to specific quantitative metrics such as follows.

Fig. 3. DJI Matrice 100 used to collect measure data [36].

1) *IC:* It evaluates the relative intensity variations in the image, providing an indication of its overall clarity and sharpness. It is defined as [55], [56]

$$IC(\boldsymbol{I}) = \frac{\sqrt{\mathbb{A}\left[(|\boldsymbol{I}| - \mathbb{A}[|\boldsymbol{I}|])^2\right]}}{\mathbb{A}[|\boldsymbol{I}|]}. \tag{27}$$

2) *COH:* It computes the similarity between two images, i.e., the resulting ISAR image $\boldsymbol{I}$ obtained with the proposed method and a reference image $\boldsymbol{I}_R$ (ideal case without missing-data). It is given by

$$\mathrm{COH}(\boldsymbol{I}, \boldsymbol{I}_R) = \frac{\left|\mathbf{1}^{\mathrm{T}}\left(\boldsymbol{I}_R \odot \boldsymbol{I}^{\star}\right)\mathbf{1}\right|}{\|\boldsymbol{I}\|_F \ \|\boldsymbol{I}_R\|_F}. \tag{28}$$

3) *NMSE:* This metric represents the normalized error between the obtained image and the reference

$$\mathrm{NMSE}(\boldsymbol{I}, \boldsymbol{I}_R) = \frac{\|\boldsymbol{I} - \boldsymbol{I}_R\|_F}{\|\boldsymbol{I}_R\|_F}. \tag{29}$$

The dataset used in this analysis is the one described in [36], which consists of wideband radar data of several drones collected in a semi-controlled environment for the frequency range 8.2–18 GHz as well as both HH and VV polarizations. The testbed included a two-port vector network analyzer (VNA) connected to a pair of identical standard horn antennas (one for transmission and one for reception). The drone under test was mounted on a fully controlled turntable, enabling a 360° rotation in azimuth with an angular step of 0.1°. For each angular position, the VNA measured the frequency response of the target, thereby allowing the extraction of high-range-resolution profiles (HRRPs). Additional processing steps, such as coherent background subtraction and range-gating, were applied as detailed in [36] to isolate a clean target response and mitigate static clutter (background) contributions.

In the following, the data pertaining to the DJI Matrice 100 (illustrated in Fig. 3), collected in HH polarization within the 13–15 GHz sub-band over a 15° azimuth rotation of the target, are employed for the ISAR processing. In particular, the Fourier transform of its HRRP for a given aspect angle provides a frequency-domain representation of the drone backscatter and can be used to emulate the received echo due to an arbitrary radar probing waveform. The response to a given transmit signal (e.g., a chirp or a cognitive spectrum-shaped pulse) can be obtained with an element-wise multiplication between the measured target spectrum and that of the transmit signal. Equivalently, in the range domain, this operation corresponds to a convolution between the target HRRP and the radar signal.

Five different situations are considered and compared as follows.

1) The *ideal* case, used as a GT, which assumes the transmission of a standard linear frequency modulated (LFM) signal (chirp) in the absence of interference. The resulting ISAR image, computed using the RD algorithm on the measured data $\boldsymbol{S}$, represents the GT.
2) The *standard* case, involving the transmission of a standard chirp in the presence of emitters operating within the same band as the ISAR frequency range, and the computation of the ISAR image using the RD algorithm applied to $\boldsymbol{S}$.
3) The *notched* case, comprising a perception stage, where the radar recognizes the presence of overlaid emitters, and an action stage, involving design (by means of Algorithm 1) and transmission of a tailored chirp-like signal with spectral notches in the frequency spectra. Here, the ISAR image is obtained by means of the RD algorithm on the collected *incomplete* data $\boldsymbol{S}$.
4) *notched + CS* case (referred to as *N-CS* case), wherein Algorithm 2 is applied to the collected incomplete data $\boldsymbol{S}$ (as also obtained in the notched case) to reconstruct the frequency-angle data, thus allowing to counter the potential resolution loss induced by the waveform spectral notches. Therefore, the ISAR image is achieved using the RD algorithm on the *reconstructed* data $\hat{\boldsymbol{S}}_c$.
5) *notched + RM* case (referred to as *N-RM* case), which is similar to the N-CS case, with the key difference of leveraging Algorithm 3 as recovery method, considering $\lambda = 300$, $\tau = 20\lambda_{\max}(\boldsymbol{\Theta}_x^{\dagger}\boldsymbol{\Theta}_x)\lambda_{\max}(\boldsymbol{\Theta}_y^{\dagger}\boldsymbol{\Theta}_y)$, and $k_{\mathrm{MAX}} = 50$.

In the aforementioned scenarios, all the overlaid sources are assumed to be telecommunication emitters (representing the only disturbance contributions), transmitting quadrature phase shift keying (QPSK) signals[4] [57].

For the aim of this analysis, the spectrum of each complex HRRP target echo signal (provided by the dataset [36] using the same preprocessing steps), for a given aspect angle θ_i (corresponding to a specific slow-time snapshot), is first multiplied by the transmitted waveform spectrum, as initial step to model (approximately) the noise-free data collected by the ISAR receiver. Subsequently, the range-domain signal, obtained following an inverse Fourier transform of the resulting spectrum, is superimposed on the interference. The resulting samples, which represent the signal measured by an actual ISAR system, undergo pulse compression with the transmitted waveform and are stored in the ith row of a range-angle data matrix. Once all the slow-time snapshots have

[4]QPSK signals are generated from random binary data with a bespoke symbol rate to control the signal bandwidth.

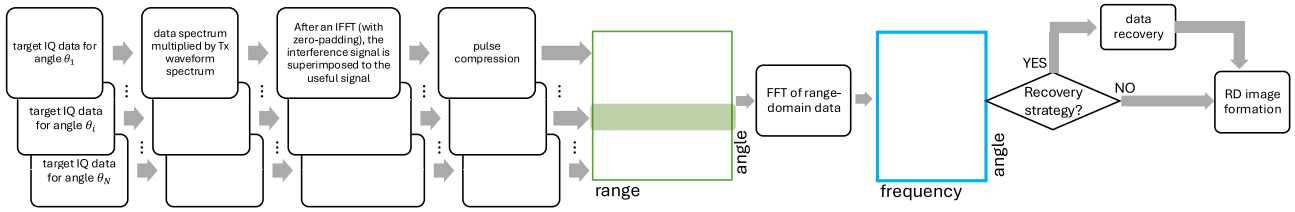

Fig. 4. Flowchart depicting the scenario generation process employed for the numerical analysis of Section IV.

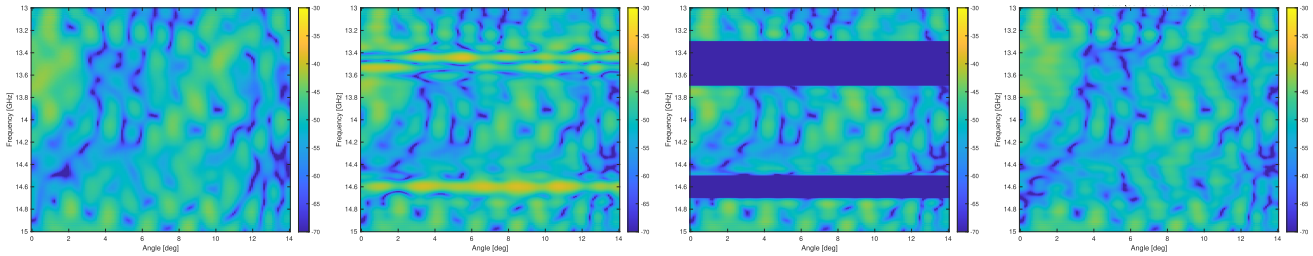

(a) (b) (c) (d)

Fig. 5. Frequency-angle (dB) spectrum in the presence of two interferers. (a) GT. (b) Standard case. (c) Notched case. (d) N-CS/N-RM case.

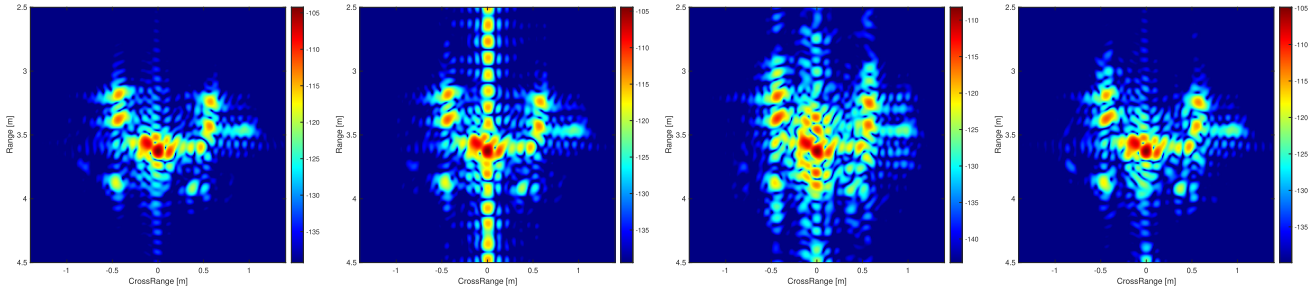

(a) (b) (c) (d)

Fig. 6. ISAR image (dB) obtained using the RD algorithm on the frequency-angle data in the presence of two interferers. (a) GT. (b) Standard case. (c) Notched case. (d) N-CS/N-RM case.

been processed, after computing the FFT of the range-domain data, the resulting frequency-angle matrix is employed for the formation of the ISAR image using the standard RD algorithm. It should be noted that in the N-CS and N-RM cases, prior to the image formation step, the data matrix undergoes a frequency-angle data recovery procedure, according to the methods detailed in Sections III-A and III-B, respectively. Finally, the obtained data experience the RD image formation. The sequence of the employed steps is illustrated in the flowchart reported in Fig. 4.

The five mentioned cases are analyzed and compared across several operational scenarios, reporting the amplitude (dB) of the frequency-time (i.e., frequency-angle) data, the corresponding ISAR image (obtained using the standard RD imaging procedure), and the aforementioned figures of merit to assess ISAR image quality. More precisely, high signal-to-noise ratio (SNR) scenarios of practical relevance are considered in Section IV-A, whereas the challenging case of spectrally compatible ISAR imaging under low SNR regime is addressed in Section IV-B.

A. High SNR Scenarios

The first scenario (Figs. 5 and 6) considers two communication sources, with the former operating in the range $[13.38, 13.62]$ GHz with a 240-MHz bandwidth, and the latter in the range $[14.53, 14.65]$ GHz with a 120-MHz bandwidth. For the synthesis of the spectrally-shaped waveform in the notched cases, Algorithm 1 is employed with $\bar{N} = 5000$ and $W = 2500$, where the considered notch depths correspond to the interference-to-noise ratio (INR) levels of the detected interferers, i.e., unless otherwise specified, 30 dB for the first notch and 40 dB for the second one, estimated during the perception stage.

The figures clearly show that, if not properly accounted for, interfering signals introduce noticeable spurious in the resulting ISAR image [Fig. 6(b)]. Employing the cognitive approach only and downstream the pulse compression, the frequency-angle data results are gapped in the frequency domain [Fig. 5(c)]. The presence of these missing data is highly damaging for the imaging process, resulting in high sidelobes appearing as fake scatterers [Fig. 6(c)]. Conversely, leveraging the CS/RM technique (the two recovery strategies achieve indistinguishable results), it is possible to reconstruct the frequency-angle data [Fig. 5(d)] and obtain an high-quality ISAR image [Fig. 6(d)], with negligible visual differences from the GT [Fig. 6(a)].

The second scenario (illustrated in Figs. 7 and 8) considers the presence of multiple emitters, each active only during

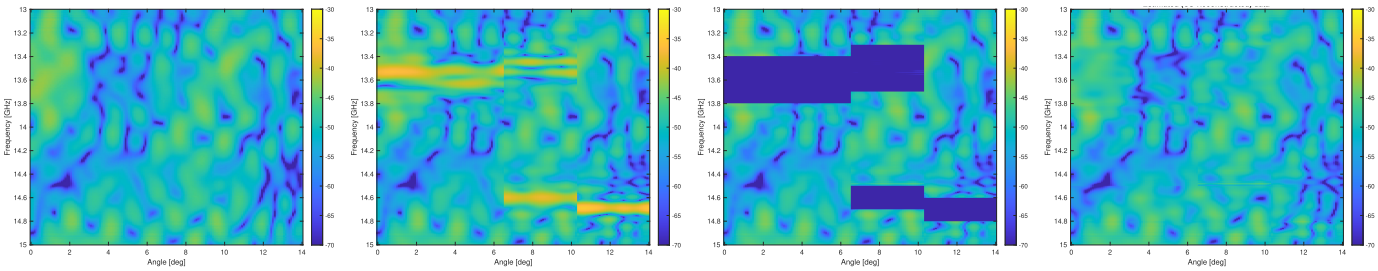

(a) (b) (c) (d)

Fig. 7. Frequency-angle (dB) spectrum in the presence of multiple emitters active in different temporal slots. (a) GT. (b) Standard case. (c) Notched case. (d) N-CS/N-RM case.

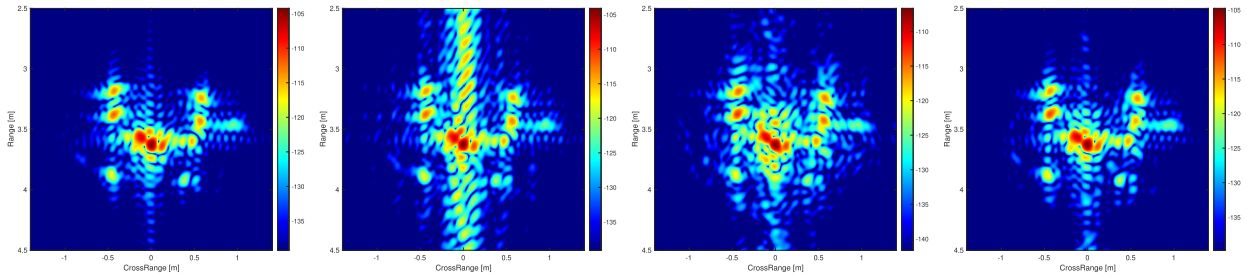

(a) (b) (c) (d)

Fig. 8. ISAR image (dB) obtained using the RD algorithm on the frequency-angle data in the presence of multiple emitters active in different temporal slots. (a) GT. (b) Standard case. (c) Notched case. (d) N-CS/N-RM case.

specific temporal slots corresponding to distinct target aspect angle intervals. Leveraging the perception-action cycle, the radar is able to adapt to the changing spectral environment. In particular, when a different spectral condition is sensed, a suitable spectrally-shaped waveform is synthesized via Algorithm 1 to ensure coexistence with the active emitters. Three different spectral environments are simulated as follows.

1) A single emitter operates in the $[13.45, 13.69]$-GHz band (240-MHz bandwidth) during the interval associated with target aspect angles in the range $[0°, 7°]$. A waveform is synthesized with a single spectral notch of 40-dB depth.
2) Two emitters are active in the subsequent interval, covering aspect angles from $[7°, 11°]$: the former transmits in the $[13.38, 13.62]$-GHz band (240-MHz bandwidth), and the latter in the $[14.53, 14.65]$-GHz band (120-MHz bandwidth). In this case, a spectrally-shaped waveform with two notches is designed, having depths of 30 and 40 dB, respectively.
3) Finally, a single emitter transmits in the $[14.665, 14.745]$-GHz band (80-MHz bandwidth) during the interval corresponding to aspect angles in the range $[11°, 15°]$. A waveform is synthesized with a single spectral notch of 40-dB depth.

Like in the previous scenario, the plots reveal that only in the N-CS/N-RM case it is possible to obtain a faithful ISAR image of the drone. As a matter of fact, in the other cases, the interference and the missing data noticeable degrade the image quality, hindering the recognition of the drone shape.

The third scenario (Figs. 9 and 10) considers a multifunction radar that performs a number of tasks, including search, track, possible imaging of multiple targets, as well as communication activities [18], [58]. Consequently, it is assumed that only 50% of the dwell time can be used for the ISAR imaging of a target, resulting in the loss of data in the slow-time dimension, in addition to those missing in the frequency domain due to the spectral notches of the cognitive waveform. This scenario further corroborates the effectiveness of the considered approach in yielding high-quality ISAR products in a contested and congested electromagnetic environment, where the use of a spectrally-shaped waveform is crucial. Furthermore, it demonstrates the potential for radar to perform additional RF operations, thereby encompassing the ISAR process within the framework of an MPAR system.

Table I reports the IC, COH, and NMSE values computed on the obtained ISAR images in all the analyzed scenarios. Inspection of the results highlights that the N-CS/N-RM framework attains the highest score for all the considered metrics, with values approaching the corresponding benchmarks. This behavior confirms the capabilities of the considered data recovery methods.

B. Low SNR Scenarios

In the following, the cognitive ISAR process is investigated in a low SNR regime, such as in the case of distant targets (still detectable) as well as in the presence of some barrage jamming[5] affecting the entire radar bandwidth. In such contexts, the observed data $\boldsymbol{S}$ is significantly corrupted by interference.

[5]The barrage jamming is modeled as circularly symmetric zero-mean complex Gaussian white noise. For the simulation of low SNR scenarios, a barrage jamming signal (whose bandwidth is larger than that of the radar) is generated with a desired power σ_J^2 and superimposed on the measured data.

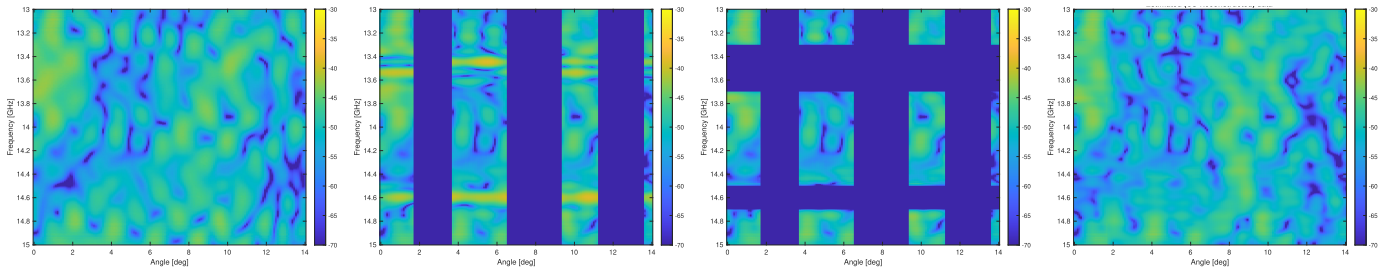

(a) (b) (c) (d)

Fig. 9. Frequency-angle (dB) spectrum for a multifunction radar in the presence of two interferers. (a) GT. (b) Standard case. (c) Notched case. (d) N-CS/N-RM case.

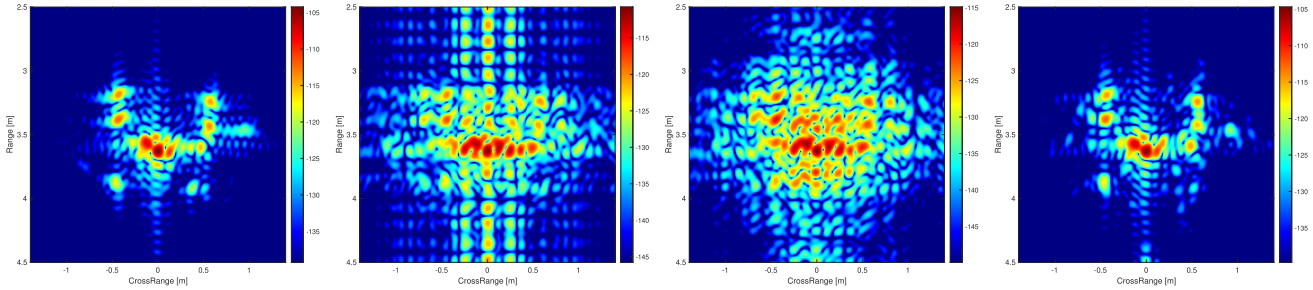

(a) (b) (c) (d)

Fig. 10. ISAR image (dB) for a multifunction radar, obtained using the RD algorithm on the frequency-angle data in the presence of two interferers. (a) GT. (b) Standard case. (c) Notched case. (d) N-CS/N-RM case.

TABLE I

IMAGE QUALITY METRICS FOR DIFFERENT SCENARIOS AND TECHNIQUES

Scenario	Case	IC	COH	NMSE
Two interferers	GT	9.44×10^{-2}	1.000	0
	Standard case	8.39×10^{-2}	9.986×10^{-1}	6.00×10^{-2}
	notched case	8.55×10^{-2}	9.987×10^{-1}	5.33×10^{-2}
	N-CS/N-RM case	$\mathbf{9.33 \times 10^{-2}}$	$\mathbf{9.994 \times 10^{-1}}$	$\mathbf{3.42 \times 10^{-2}}$
Multiple interferers active in different temporal slots	GT	9.44×10^{-2}	1.000	0
	Standard case	7.76×10^{-2}	9.980×10^{-1}	8.26×10^{-2}
	notched case	8.24×10^{-2}	9.988×10^{-1}	5.40×10^{-2}
	N-CS/N-RM	$\mathbf{8.98 \times 10^{-2}}$	$\mathbf{9.994 \times 10^{-1}}$	$\mathbf{3.48 \times 10^{-2}}$
MPAR in the presence of two interferers	GT	9.44×10^{-2}	1.000	0
	Standard case	6.72×10^{-2}	9.976×10^{-1}	8.64×10^{-2}
	notched case	7.31×10^{-2}	9.982×10^{-1}	6.47×10^{-2}
	N-CS/N-RM	$\mathbf{9.00 \times 10^{-2}}$	$\mathbf{9.990 \times 10^{-1}}$	$\mathbf{4.51 \times 10^{-2}}$

Fig. 11 reports the ISAR images obtained under various approaches, assuming a single-pulse SNR (after compression) of −7 dB. The results show that, in both the standard and notched cases, the target signal is overwhelmed by the disturbance, resulting in practically unusable images. Even the CS-based ISAR method, while capable of recovering missing data induced by spectral notches, fails to produce a high-quality image, as evidenced by the presence of spurious scatterers.

In contrast, the proposed N-RM approach demonstrates a strong ability to suppress interference and yield a faithful image of the target. This performance stems from the adopted RM framework, which enables the reconstruction of slow-time/frequency data by leveraging only the dominant modes in the scene.

Furthermore, the image quality, in terms of IC, COH, and NMSE metrics, achieved by the diverse approaches is illustrated in Figs. 12–14, respectively, for SNR values ranging from −11 to 19 dB.

Inspection of the curves highlights that the proposed N-RM technique consistently outperforms its counterparts in terms of image fidelity, as reflected by the higher COH and lower NMSE values attained across the entire SNR range. As compared to IC, N-RM achieves the highest performance for SNR greater than 5 dB, while at lower values, in the standard and N-CS cases, a slightly higher contrast is obtained. However, it is worth remarking that IC solely measures image sharpness and does not reflect fidelity to the GT.

Overall, the proposed missing-data retrieval strategies exhibit a robust performance in a variety of practical scenar-

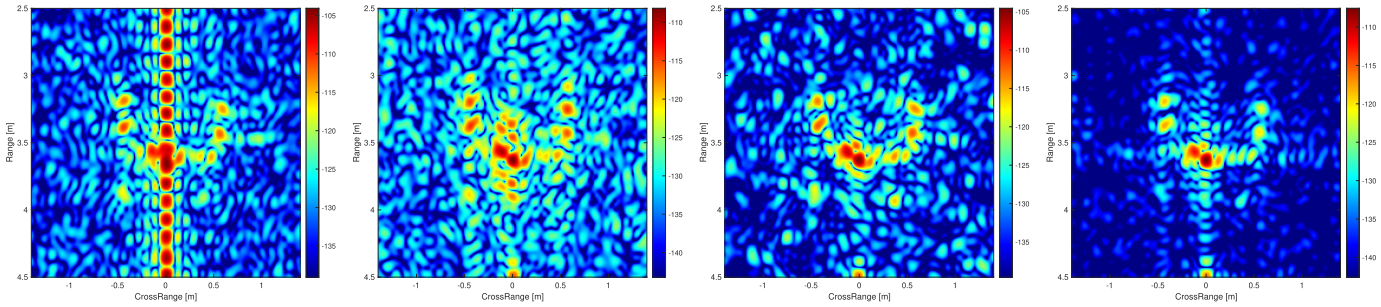

(a) (b) (c) (d)

Fig. 11. ISAR image (dB) obtained using the RD algorithm on the frequency-angle data in the presence of two interferers and SNR = −7 dB. (a) Standard case. (b) Notched case. (c) N-CS case. (d) N-RM case.

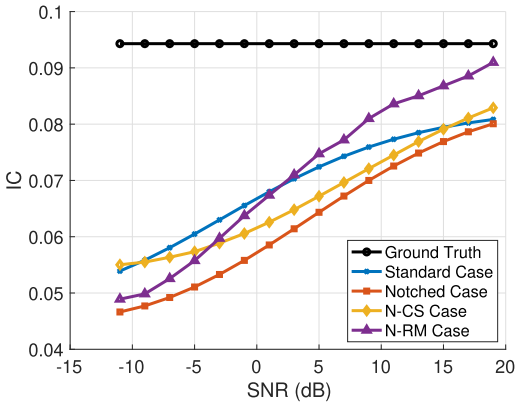

Fig. 12. IC versus SNR in the presence of two interferers.

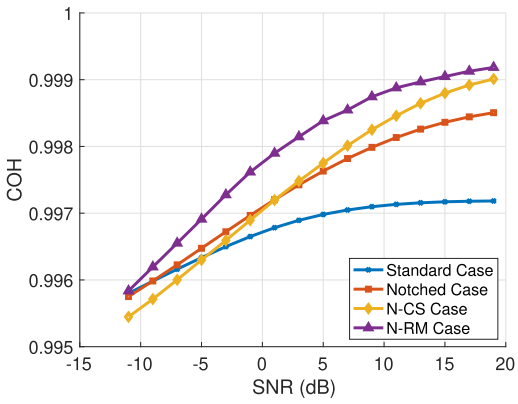

Fig. 13. COH versus SNR in the presence of two interferers.

ios, with the N-RM technique being particularly effective in challenging low-SNR conditions.

V. Conclusion

In this article, a cognitive ISAR system designed to guarantee spectral compatibility with possible overlaid emitters has been proposed. To this end, the radar alternates between perception and action stages, exploiting a spectrum sensing unit to recognize potential emitters within its frequency range and a tailored waveform design process to synthesize radar imaging waveforms with spectral notches used to probe the environment. A crucial aspect of the proposed architecture is the ability to yield high-quality ISAR images by mitigating the effects of missing data both in the frequency domain, due to spectral notches in the transmitted

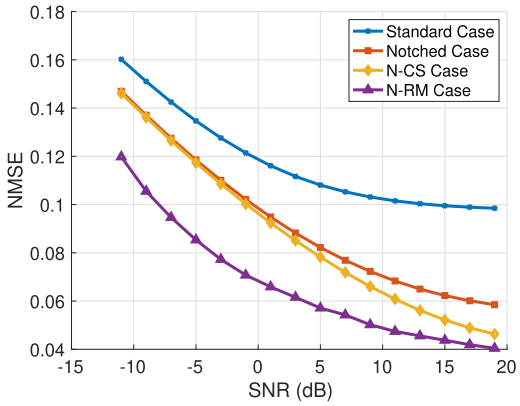

Fig. 14. NMSE versus SNR in the presence of two interferers.

waveform, and possibly in the slow-time dimension, due to the interrupted mode induced by higher priority tasks in an MPAR system. Therefore, a data recovery process is performed prior to the image formation step, either via the CS framework or by solving an RM problem. Extensive numerical analyses, based on drone measurements in the [13, 15]-GHz band, have shown that the proposed system is capable of ensuring spectral compatibility while delivering high-quality ISAR images. Several operating scenarios, including multiple communication sources, multiple emitters active in different temporal slots, as well as a multifunction radar operation, have been considered. The experimental results have shown that the developed strategies allow to produce faithful ISAR images that are visually comparable to the GT and effectively maximize standard image quality metrics in several challenging scenarios of practical relevance. Notably, the N-RM method stands out for its high reconstruction accuracy and robustness in challenging scenarios, making it a promising enabler for advanced cognitive-based applications in both civilian and military domains.

Future research studies might involve the application and validation of the proposed technique on additional datasets, as well as a detailed performance analysis under a nonideal perception stage, where the estimated sources' spectral parameters may be inaccurate. Moreover, it will be worth extending the framework to different architectures, such as multistatic and/or polarimetric ISAR systems. Finally, it would be of interest to generalize the RM recovery process employing the Schatten norm in lieu of the plain nuclear norm.

Data Availability Statement

Data supporting this study cannot be made available due to commercial restrictions.

References

[1] M. Rosamilia, A. Aubry, A. Balleri, A. De Maio, and M. Martorella, "A cognitive-based ISAR system for spectral compatibility applications," in *Proc. IEEE Int. Workshop Technol. Defense Secur. (TechDefense)*, Nov. 2024, pp. 74–79.

[2] A. Aubry, V. Carotenuto, A. De Maio, A. Farina, and L. Pallotta, "Optimization theory-based radar waveform design for spectrally dense environments," *IEEE Aerosp. Electron. Syst. Mag.*, vol. 31, no. 12, pp. 14–25, Dec. 2016.

[3] S. D. Blunt, J. G. Metcalf, C. R. Biggs, and E. Perrins, "Performance characteristics and metrics for intra-pulse radar-embedded communication," *IEEE J. Sel. Areas Commun.*, vol. 29, no. 10, pp. 2057–2066, Dec. 2011.

[4] G. T. Capraro, C. T. Capraro, M. C. Wicks, and R. A. Liuzzi, "Artificial intelligence and waveform diversity," in *Proc. Manag. Technol. Driven Org., Hum. Side Innov. Change*, Jun. 2003, pp. 270–274.

[5] M. C. Wicks and P. Antonik, "Waveform diversity in intelligent sensor systems," in *Proc. IET Forum Waveform Diversity Design Commun., Radar Sonar*, 2006, pp. 1–6.

[6] F. Gini, A. De Maio, and L. Patton, *Waveform Design and Diversity for Advanced Radar Systems*. London, U.K.: IET, 2012.

[7] G. Cui, A. De Maio, A. Farina, and J. Li, *Radar Waveform Design Based on Optimization Theory*. London, U.K.: IET, 2020.

[8] A. Aubry, V. Carotenuto, A. De Maio, and M. A. Govoni, "Multi-snapshot spectrum sensing for cognitive radar via block-sparsity exploitation," *IEEE Trans. Signal Process.*, vol. 67, no. 6, pp. 1396–1406, Mar. 2019.

[9] A. Aubry, V. Carotenuto, A. De Maio, M. A. Govoni, and A. Farina, "Experimental analysis of block-sparsity-based spectrum sensing techniques for cognitive radar," *IEEE Trans. Aerosp. Electron. Syst.*, vol. 57, no. 1, pp. 355–370, Feb. 2021.

[10] H. He, P. Stoica, and J. Li, "Waveform design with stopband and correlation constraints for cognitive radar," in *Proc. 2nd Int. Workshop Cognit. Inf. Process.*, Jun. 2010, pp. 344–349.

[11] I. W. Selesnick and S. U. Pillai, "Chirp-like transmit waveforms with multiple frequency-notches," in *Proc. IEEE RadarCon (RADAR)*, May 2011, pp. 1106–1110.

[12] M. Piezzo, A. De Maio, A. Aubry, and A. Farina, "Cognitive radar waveform design for spectral coexistence," in *Proc. IEEE Radar Conf. (RadarCon)*, Apr. 2013, pp. 1–4.

[13] R. A. Romero and K. D. Shepherd, "Friendly spectrally shaped radar waveform with legacy communication systems for shared access and spectrum management," *IEEE Access*, vol. 3, pp. 1541–1554, 2015.

[14] A. Aubry, V. Carotenuto, and A. De Maio, "Forcing multiple spectral compatibility constraints in radar waveforms," *IEEE Signal Process. Lett.*, vol. 23, no. 4, pp. 483–487, Apr. 2016.

[15] A. Farina, A. De Maio, and S. Haykin, *The Impact of Cognition on Radar Technology* (Radar, Sonar & Navigation). London, U.K.: Inst. Eng. Technol., 2017.

[16] A. Aubry, A. De Maio, M. A. Govoni, and L. Martino, "On the design of multi-spectrally constrained constant modulus radar signals," *IEEE Trans. Signal Process.*, vol. 68, pp. 2231–2243, 2020.

[17] A. Aubry, P. Babu, A. De Maio, and L. Pallotta, "Off-grid multisnapshot spectrum sensing for cognitive radar," *IEEE Trans. Aerosp. Electron. Syst.*, vol. 61, no. 4, pp. 1–18, Aug. 2025.

[18] A. Aubry, A. De Maio, and L. Pallotta, "A priority-based scheduling scheme for search, track, and communications in MPARs," *IEEE Trans. Radar Syst.*, vol. 2, pp. 471–481, 2024.

[19] W. Qiu et al., "Compressive sensing–based algorithm for passive bistatic ISAR with DVB-T signals," *IEEE Trans. Aerosp. Electron. Syst.*, vol. 51, no. 3, pp. 2166–2180, Jul. 2015.

[20] S. Tomei, A. Bacci, E. Giusti, M. Martorella, and F. Berizzi, "Compressive sensing-based inverse synthetic radar imaging imaging from incomplete data," *IET Radar, Sonar Navigat.*, vol. 10, no. 2, pp. 386–397, Feb. 2016.

[21] A. Bacci, D. Staglianò, E. Giusti, S. Tomei, F. Berizzi, and M. Martorella, "Compressive sensing for interferometric inverse synthetic aperture radar applications," *IET Radar, Sonar Navigat.*, vol. 10, no. 8, pp. 1446–1457, Oct. 2016.

[22] A. Ghaffari, M. Babaie-Zadeh, and C. Jutten, "Sparse decomposition of two dimensional signals," in *Proc. IEEE Int. Conf. Acoust., Speech Signal Process.*, Apr. 2009, pp. 3157–3160.

[23] T. Blumensath and M. E. Davies, "Iterative hard thresholding for compressed sensing," *Appl. Comput. Harmon. Anal.*, vol. 27, no. 3, pp. 265–274, Nov. 2009.

[24] D. Needell and J. A. Tropp, "CoSaMP: Iterative signal recovery from incomplete and inaccurate samples," *Appl. Comput. Harmon. Anal.*, vol. 26, no. 3, pp. 301–321, May 2009.

[25] J. A. Tropp and A. C. Gilbert, "Signal recovery from random measurements via orthogonal matching pursuit," *IEEE Trans. Inf. Theory*, vol. 53, no. 12, pp. 4655–4666, Dec. 2007.

[26] F. E. Rezagah, S. Jalali, E. Erkip, and H. V. Poor, "Compression-based compressed sensing," *IEEE Trans. Inf. Theory*, vol. 63, no. 10, pp. 6735–6752, Oct. 2017.

[27] D. L. Donoho, "Compressed sensing," *IEEE Trans. Inf. Theory*, vol. 52, no. 4, pp. 1289–1306, Apr. 2006.

[28] M. Fazel, E. Candes, B. Recht, and P. Parrilo, "Compressed sensing and robust recovery of low rank matrices," in *Proc. 42nd Asilomar Conf. Signals, Syst. Comput.*, Oct. 2008, pp. 1043–1047.

[29] B. Recht, M. Fazel, and P. A. Parrilo, "Guaranteed minimum-rank solutions of linear matrix equations via nuclear norm minimization," *SIAM Rev.*, vol. 52, no. 3, pp. 471–501, Jan. 2010.

[30] G. Peyré and J. Fadili, "Group sparsity with overlapping partition functions," in *Proc. 19th Eur. Signal Process. Conf.*, Aug. 2011, pp. 303–307.

[31] L. Liu, W. Huang, and D.-R. Chen, "Exact minimum rank approximation via schattenp-norm minimization," *J. Comput. Appl. Math.*, vol. 267, pp. 218–227, Sep. 2014.

[32] W. Qiu et al., "Compressive sensing for passive ISAR with DVB-T signal," in *Proc. 14th Int. Radar Symp. (IRS)*, vol. 1, Jun. 2013, pp. 113–118.

[33] T. T. Wu and K. Lange, "The MM alternative to EM," *Stat. Sci.*, vol. 25, no. 4, pp. 492–505, 2010, doi: 10.1214/08-STS264.

[34] D. R. Hunter and K. Lange, "A tutorial on MM algorithms," *Amer. Statistician*, vol. 58, no. 1, pp. 30–37, Feb. 2004.

[35] Y. Sun, P. Babu, and D. P. Palomar, "Majorization-minimization algorithms in signal processing, communications, and machine learning," *IEEE Trans. Signal Process.*, vol. 65, no. 3, pp. 794–816, Feb. 2017.

[36] M. Rosamilia, A. Balleri, A. De Maio, A. Aubry, and V. Carotenuto, "Radar detection performance prediction using measured UAVs RCS data," *IEEE Trans. Aerosp. Electron. Syst.*, vol. 59, no. 4, pp. 3550–3565, Aug. 2023.

[37] M. Rosamilia, A. Aubry, A. Balleri, V. Carotenuto, and A. De Maio, "Radar detection performance via frequency agility using measured UAVs RCS data," *IEEE Sensors J.*, vol. 23, no. 19, pp. 23011–23019, Oct. 2023.

[38] O. Roy and M. Vetterli, "The effective rank: A measure of effective dimensionality," in *Proc. 15th Eur. Signal Process. Conf. (EUSIPCO)*, Sep. 2007, pp. 606–610.

[39] V. Carotenuto, A. Aubry, A. De Maio, N. Pasquino, and A. Farina, "Assessing agile spectrum management for cognitive radar on measured data," *IEEE Aerosp. Electron. Syst. Mag.*, vol. 35, no. 6, pp. 20–32, Jun. 2020.

[40] A. Martone and M. Amin, "A view on radar and communication systems coexistence and dual functionality in the era of spectrum sensing," *Digit. Signal Process.*, vol. 119, Dec. 2021, Art. no. 103135.

[41] M. Rosamilia, A. Aubry, V. Carotenuto, and A. De Maio, "Cognitive noncoherent jamming techniques for frequency selective attacks," *IEEE Trans. Aerosp. Electron. Syst.*, vol. 61, no. 5, pp. 14330–14343, Oct. 2025.

[42] V. Chen and M. Martorella, *Inverse Synthetic Aperture Radar Imaging: Principles, Algorithms and Applications*. London, U.K.: IET, 2014.

[43] E. Giusti, S. Tomei, A. Bacci, M. Martorella, and F. Berizzi, "Autofocus for CS based ISAR imaging in the presence of gapped data," in *Proc. Workshop Compressive Sensng Appl. to Radar (CoSeRa)*, 2013, pp. 1–4.

[44] M. Martorella, F. Berizzi, and B. Haywood, "Contrast maximisation based technique for 2-D ISAR autofocusing," *IEE Proc.-Radar, Sonar Navigat.*, vol. 152, no. 4, pp. 253–262, Aug. 2005.

[45] H. Zare and M. Hajarian, "Determination of regularization parameter via solving a multi-objective optimization problem," *Appl. Numer. Math.*, vol. 156, pp. 542–554, Oct. 2020.

[46] F. Bauer and M. A. Lukas, "Comparingparameter choice methods for regularization of ill-posed problems," *Math. Comput. Simul.*, vol. 81, no. 9, pp. 1795–1841, May 2011.

[47] Z. Chen, J. Tang, X. Y. Zhang, D. K. C. So, S. Jin, and K.-K. Wong, "Hybrid evolutionary-based sparse channel estimation for IRS-assisted mmWave MIMO systems," *IEEE Trans. Wireless Commun.*, vol. 21, no. 3, pp. 1586–1601, Mar. 2022.
[48] S. Boyd and L. Vandenberghe, *Convex Optimization*. Cambridge, U.K.: Cambridge Univ. Press, 2004.
[49] A. De Maio, Y. C. Eldar, and A. M. Haimovich, *Compressed Sensing in Radar Signal Processing*. Cambridge, U.K.: Cambridge Univ. Press, 2019.
[50] E. J. Candes and T. Tao, "The power of convex relaxation: Near-optimal matrix completion," *IEEE Trans. Inf. Theory*, vol. 56, no. 5, pp. 2053–2080, May 2010.
[51] M. Fazel, "Matrix rank minimization with applications," Ph.D. dissertation, Dept. Elect. Eng., Stanford University, Stanford, CA, USA, 2002.
[52] M. Razaviyayn, M. Hong, and Z.-Q. Luo, "A unified convergence analysis of block successive minimization methods for nonsmooth optimization," *SIAM J. Optim.*, vol. 23, no. 2, pp. 1126–1153, Jan. 2013.
[53] A. Aubry, A. De Maio, A. Zappone, M. Razaviyayn, and Z.-Q. Luo, "A new sequential optimization procedure and its applications to resource allocation for wireless systems," *IEEE Trans. Signal Process.*, vol. 66, no. 24, pp. 6518–6533, Dec. 2018.
[54] R. A. Horn and C. R. Johnson, *Matrix Analysis*. Cambridge, U.K.: Cambridge Univ. Press, 2012.
[55] F. Berizzi and G. Corsini, "Autofocusing of inverse synthetic aperture radar images using contrast optimization," *IEEE Trans. Aerosp. Electron. Syst.*, vol. 32, no. 3, pp. 1185–1191, Jul. 1996.
[56] J. Cai, M. Martorella, S. Chang, Q. Liu, Z. Ding, and T. Long, "Efficient nonparametric ISAR autofocus algorithm based on contrast maximization and Newton's method," *IEEE Sensors J.*, vol. 21, no. 4, pp. 4474–4487, Feb. 2021.
[57] A. F. Molisch, *Wireless Communications*, vol. 34. Hoboken, NJ, USA: Wiley, 2012.
[58] A. Aubry, A. De Maio, and L. Pallotta, "Power-aperture resource allocation for a MPAR with communications capabilities," *IEEE Trans. Veh. Technol.*, vol. 73, no. 6, pp. 7474–7488, Jun. 2024.

Massimo Rosamilia (Member, IEEE) received the B.S. (cum laude) and M.S. degrees in computer engineering from the University of Salerno, Fisciano, Italy, in 2017 and 2019, respectively, and the Ph.D. degree (cum laude) in information technologies and electrical engineering from the University of Naples Federico II, Naples, Italy, in 2023.

From September to November 2021, he was a Visiting Ph.D. Student at Cranfield University, Shrivenham, U.K. From September to December 2022, he was a Visiting Ph.D. Student at the University of Luxembourg, Esch-sur-Alzette, Luxembourg. From June to August 2024, he was a Visiting Researcher at the University of Birmingham, Birmingham, U.K., and from July to August 2025, he was a Visiting Researcher at Cranfield University, Shrivenham, U.K. He is currently an Assistant Professor (RTD-A) with the Department of Electrical Engineering and Information Technology (DIETI), University of Naples Federico II. His research interests include array signal processing as well as detection, estimation, and optimization theory in the context of radar systems.

Dr. Rosamilia was the recipient of the 2023 GTTI Ph.D. award for Ph.D. theses in the field of communication technologies and also the co-recipient of the SET Panel Best Paper Award (Young Scientist) at the NATO SET-319 Specialists' Meeting on "New Mathematical Frontiers for Multi-Dimensional Radar Systems", in 2023. He is currently serving as Associate Editor of the IEEE *AESS Magazine*.

Augusto Aubry (Senior Member, IEEE) received the Dr. Eng. degree (Hons.) in telecommunication engineering and the Ph.D. degree in electronic and telecommunication engineering from the University of Naples Federico II, Naples, Italy, in 2007 and 2011, respectively.

From February 2012 to April 2012, he was a Visiting Researcher with Hong Kong Baptist University, Hong Kong. He is currently an Associate Professor with the University of Naples Federico II. His research interests include statistical signal processing and optimization theory, with an emphasis on MIMO communications and radar signal processing.

Dr. Aubry was a co-recipient of the 2013 Best Paper Award (titled to B. Carlton) of IEEE TRANSACTION ON AEROSPACE AND ELECTRONIC SYSTEMS with the contribution "Knowledge-Aided (Potentially Cognitive) Transmit Signal and Receive Filter Design in Signal-Dependent Clutter". He was a recipient of the 2022 IEEE Fred Nathanson Memorial Award as the Young (less than 40 years of age) AESS Radar Engineer 2022, with the following citation for "outstanding contributions to the application of modern optimization theory to radar waveform design and adaptive signal processing."

Alessio Balleri (Senior Member, IEEE) received the Laurea degree in telecommunication engineering (summa cum laude) (five legal years) from the University of Pisa, Pisa, Italy, in 2004, and the Ph.D. degree in electronic and electrical engineering from the University College London (UCL), London, U.K., in 2010.

From February 2010 to March 2012, he was a Research Associate in Radar Systems with the Department of Electronic and Electrical Engineering, UCL. From June 2004 to December 2004, he was a Visiting Research Scholar with the Department of Electrical and Computer Engineering, University of Illinois at Chicago. He is currently a Professor of Radar Systems with Cranfield University, Shrivenham, U.K. His research interests include radar and sonar system design, biologically inspired radar and sonar systems, adaptive radar, radar and sonar target classification, target feature extraction, and modeling of radar clutter.

Dr. Balleri Guest Coedited special issues on "Biologically Inspired Radar and Sonar Systems" (2012) and "Electronic Attack and Protection for Modern Radar Systems and Radar Networks" (2024) for the IET Radar, Sonar & Navigation and a special issue on "Emerging Radar Techniques" for the EURASIP Journal on Advances in Signal Processing in 2013. He was the Technical Program Committee Co-Chair for the IET International Radar Conference 2017, Belfast, U.K., and the Technical Co-Chair of the 2020 IEEE International Radar Conference, Washington, DC, USA. He is currently serving as the Deputy Editor in Chief for the *IET Radar*, *Sonar* & *Navigation Journal*, as the Associate Editor in Chief for the IEEE *Aerospace and Electronic Systems Magazine*, and he is an elected member of the IEEE AESS Radar System Panel.

Antonio De Maio (Fellow, IEEE) received the Dr.Eng. (Hons.) and Ph.D. degrees in information engineering from the University of Naples Federico II, Naples, Italy, in 1998 and 2002, respectively.

From October 2004 to December 2004, he was a Visiting Researcher with U.S. Air Force Research Laboratory, Rome, NY, USA. From November 2007 to December 2007, he was a Visiting Researcher with The Chinese University of Hong Kong, Hong Kong. He is currently a Professor with the University of Naples Federico II. His research interests include statistical signal processing, with an emphasis on radar detection, optimization theory applied to radar signal processing, and multiple-access communications.

Dr. De Maio was a recipient of the 2010 IEEE Fred Nathanson Memorial Award as the Young (less than 40 years of age) AESS Radar Engineer 2010, whose performance is particularly noteworthy as evidenced by contributions to the radar art over a period of several years, with the following citation for "robust CFAR detection, knowledge-based radar signal processing, and waveform design and diversity." He was a co-recipient of the 2013 Best Paper Award (titled to B. Carlton) of IEEE TRANSACTIONS ON AEROSPACE AND ELECTRONIC SYSTEMS with the contribution "Knowledge- Aided (Potentially Cognitive) Transmit Signal and Receive Filter Design in Signal-Dependent Clutter." He was also a recipient of the 2024 IEEE Warren White Award for outstanding achievements due to a major technical advance (or series of advances) in the art of radar engineering, with the citation for "Contributions to Radar Signal Processing Techniques for Target Detection, Waveform Design, and Electronic Protection."

Marco Martorella (Fellow, IEEE) received the Laurea degree (bachelor's+master's) in telecommunication engineering (cum laude) from the University of Pisa, Pisa, Italy, in 1999, and the Ph.D. degree in remote sensing from the University of Pisa, in 2003.

He is now a Professor with the School of Engineering, University of Birmingham, where he is Head of the Microwave Integrated Systems Laboratory (MISL) and Director of the Communications and Sensing Cluster. He is also Chair of the NATO Sensors and Electronics Technology (SET) Panel and Vice-Director at the Radar and Surveillance Systems (RaSS) National Laboratory, Pisa. He is author of about 300 international journal and conference papers, four books and more than 20 book chapters. He has chaired several NATO research activities, including the SET-293 RTG on "RF Sensing for Space Situational Awareness" and the SET-250 RTG on "Multi-dimensional Radar Imaging," one Exploratory Team and three Specialist Meetings on imaging- and space- related themes. He is a Co-Founder of ECHOES, a radar systems-related spin-off company. His research interests are mainly in the field of radar, with specific focus on radar imaging, multidimensional radar, passive radar and space situational awareness.

Dr. martorella has been recipient of the IEEE 2013 Fred Nathanson Memorial Radar Award, the 2016 Outstanding Information Research Foundation Book publication, four NATO SET Panel Excellence Awards (2017, 2018, 2021 and 2023) and two NATO STO Excellence Award (2022 and 2024).

https://dspace.org/

Exploiting cognition in ISAR processing for spectral compatibility applications

Rosamilia, Massimo; Aubry, Augusto; Balleri, Alessio; De Maio, Antonio; Martorella, Marco

2026
Institute of Electrical and Electronics Engineers (IEEE)
https://doi.org/10.1109/trs.2025.3645384
Rosamilia M, Aubry A, Balleri A, et al., (2026) Exploiting cognition in ISAR processing for spectral compatibility applications. IEEE Transactions on Radar Systems, Volume 4, 2026, pp. 194-206

Downloaded from a DSpace repository. https://dspace.org/